GA–A27441

ADVANCES IN THE PHYSICS UNDERSTANDING OF ELM SUPPRESSION USING RESONANT MAGNETIC PERTURBATIONS IN DIII-D

by
M.R. WADE, R. NAZIKIAN, D. BATTAGLIA, R.J. BUTTERY, J.S. deGRASSIE, T.E. EVANS, M.E. FENSTERMACHER, N.M. FERRARO, B.A. GRIERSON, J.M. HANSON, M.J. LANCTOT, G.R. McKEE, R.A. MOYER, D.M. ORLOV, W.M. SOLOMON, O. SCHMITZ, M.W. SHAFER, P.B. SNYDER, E.A. UNTERBERG,A. WINGEN, and L. ZENG

OCTOBER 2012

GENERAL ATOMICS

DISCLAIMER

GA–A27441

ADVANCES IN THE PHYSICS UNDERSTANDING OF ELM SUPPRESSION USING RESONANT MAGNETIC PERTURBATIONS IN DIII-D

by
M.R. WADE, R. NAZIKIAN,* D. BATTAGLIA,* R.J. BUTTERY, J.S. deGRASSIE, T.E. EVANS, M.E. FENSTERMACHER,† N.M. FERRARO, B.A. GRIERSON,* J.M. HANSON,‡ M.J. LANCTOT,† G.R. McKEE,# R.A. MOYER,¶ D.M. ORLOV,¶ W.M. SOLOMON,* O. SCHMITZ,§ M.W. SHAFER,° P.B. SNYDER, E.A. UNTERBERG,° A. WINGEN,° and L. ZENG◊

This is a preprint of a paper to be presented at the Twenty-fourth IAEA Fusion Energy Conf., October 8-13, 2012 in San Diego, California.

*Princeton Plasma Physics Laboratory, Princeton, New Jersey, USA.
†Lawrence Livermore Laboratory, Livermore, California, USA.
‡Columbia University, New York, New York, USA.
#University of Wisconsin-Madison, Madison, Wisconsin, USA.
¶University of California San Diego, La Jolla, California, USA.
§Forschungzentrum Juelich, Juelich, Germany.
°University of California Los Angeles, Los Angeles, California, USA.

Work supported in part by
the U.S. Department of Energy
under DE-FC02-04ER54698, DE-AC02-09CH11466, DE-FG02-89ER53296, DE-FG02-08ER54999, DE-FG02-07ER54917, and DE-FG02-08ER54984

GENERAL ATOMICS PROJECT 30200
OCTOBER 2012

GENERAL ATOMICS

Advances in the Physics Understanding of ELM Suppression Using Resonant Magnetic Perturbations in DIII-D

M.R. Wade 1), R. Nazikian 2), D. Battaglia 2), R.J. Buttery 1), J.S. deGrassie 1), T.E. Evans 1), M.E. Fenstermacher 3), N.M. Ferraro 1), B.A. Grierson 2), J.M. Hansen 4), M.J. Lanctot 3), G.R. McKee 5), R.A. Moyer 6), D.M. Orlov 6), W.M. Solomon 2), O. Schmitz 7), M.W. Shafer 8), P.B. Snyder 1), E.A. Unterberg 8), A. Wingen 8), and L. Zeng 9)
email: wade@fusion.gat.com

1) General Atomics, San Diego, California 92186-5608, USA
2) Princeton Plasma Physics Laboratory, Princeton, New Jersey 08543-0451, USA
3) Lawrence Livermore National Laboratory, Livermore, California 94550, USA
4) Columbia University, New York, New York 10027, USA
5) University of Wisconsin, Madison, Wisconsin 53706, USA
6) University of California San Diego, La Jolla, California 92093-0417, USA
7) Forschungszentrum Jülich GmbH, Association EURATOM-FZJ, Tilateral Euregio Cluster, Jülich, Germany
8) Oak Ridge National Laboratory, Oak Ridge, Tennessee 37831, USA
9) University of California Los Angeles, Los Angeles, California 90095-7099, USA

Abstract. Recent experiments on DIII-D have increased confidence in the ability to suppress edge localized modes (ELMs) using resonant magnetic perturbations (RMPs) in ITER, including an improved physics basis for the edge response to RMPs as well as expansion of RMP ELM suppression to more ITER-like conditions. ELM suppression has been achieved utilizing n=3 RMPs in the ITER baseline scenario for long durations (~3.5 s) and expanded to include dominantly helium plasmas and the use of n=2 RMPs. Utilizing RMP phase and amplitude modulations to enhance measurement range and fidelity, a complex plasma response has been revealed including lobe structures in the divertor, kink-like displacements at the edge, and apparent displacement inversions as well as enhanced turbulence at the pedestal top. The consistency of these observations and associated plasma response modeling with an emerging model for RMP ELM suppression is discussed.

1. Introduction

Edge localized mode (ELM) control is a critical issue for ITER as the energy pulse anticipated with unmitigated ELMs is expected to severely limit the lifetime of plasma facing components [1]. Motivated by previous results from DIII-D [2], the present ITER design allows for the inclusion of magnetic coils internal to the vacuum vessel to apply resonant magnetic perturbations (RMPs) for ELM control. The specifications for the internal coils for ITER are based on empirical correlations of ELM suppression in DIII-D with vacuum modeling of presumed island generation in the edge plasma [3]. However, it is important to build confidence in the applicability of these results to the ITER baseline, with a deeper understanding of the physics mechanisms involved. Extensive studies have been made on DIII-D to confront these challenges. The extension of operational range has been explored by varying the n=3 and n=2 harmonic content. Perturbative experiments have been used to elucidate the plasma response, deploying a range of innovative profile, 2D and 3D diagnostic techniques. These experimental observations have been compared with 3D simulations using comprehensive two-fluid and field-line tracing numerical models to elucidate the key physics. From this research, a model is emerging that posits that an enhanced MHD response at the top of the pedestal limits the growth of the pedestal, thereby avoiding the peeling-ballooning stability boundary.

2. Expansion of RMP ELM Suppression to ITER-like Conditions

RMP ELM suppression has been demonstrated in the ITER baseline scenario with I/aB=1.41, β_N~1.8, H_{98y2}~0.9, and $\nu^*_{e\,ped}$=0.05 utilizing the ITER-design plasma cross section scaled down by a factor of 3.7. ELM suppression was achieved in this case utilizing one toroidal row of the two-row I-coil system in DIII-D configured for an n=3 RMP application. The use of one toroidal row instead of two is based on observations that the q_{95} window for ELM suppression in DIII-D is more readily extended to the concomitant ITER q_{95} target values with single row operation. This effect is not well understood as analysis suggests only modest changes to the resonant components of the applied field

between single and double rows. In the case shown in Fig. 1, an I-coil current of ~6 kA was applied in an n=3 configuration starting at 3.0 s. As evidenced by the D_α signal in Fig. 1(c), ELM mitigation occurs immediately with full ELM suppression achieved by 3.5 s. ELM suppression is sustained for 3.5 s (~45 τ_E). The use of electron cyclotron current drive (ECCD) broadly distributed near the q=1.5 surface was important in avoiding growth of an m=3/n=2 tearing mode. Feedback control of the neutral beams maintains β_N~1.8 through the ELM suppressed phase. The application of the electron cyclotron current drive and RMP causes a significant drop in confinement (H_{98y2}~ 1.1→0.75); however, by the end of the ELM suppressed phase, H_{98y2}=0.9 is sustained for over 1.5 s. The decrease in confinement due to the RMP is larger than typically seen with two-row I-coil RMPs, likely due to the increase in low m non-resonant components of the applied field that penetrate well into the core region. Improved performance may be expected in ITER, which will use n=4 fields that are more edge localized. Nevertheless, the results in Fig. 1 are indicative that RMP ELM suppression can be obtained in the ITER baseline scenario.

Recent experiments have also shown that n=3 RMP ELM suppression can be obtained in plasmas with a significant helium concentration f_{He}= n_{He}/n_e. These experiments utilized a discharge with q_{95}=3.4, β_N~1.7 in an ITER-similar shape in which n=3 RMP ELM suppression is typically observed in deuterium plasmas. Taking advantage of the natural decrease of f_{He}= n_{He}/n_e following boronization, f_{He} was scanned from ~35% to ~10% over 10 repeat discharges. Figure 2 shows that ELM suppression was not achieved until f_{He}<~25%. However, there is a strong correlation between the density and f_{He}, making it unclear what is the dominant variable in the ELM suppression. Attempts to raise f_{He} by gas injection invariably increased the density and brought the return of ELMs. Argon frosting of the cryopump can be used in future experiments to decouple f_{He}, n_e and $\nu^*_{e\,ped}$ (which is ~0.1 at the onset of suppression).

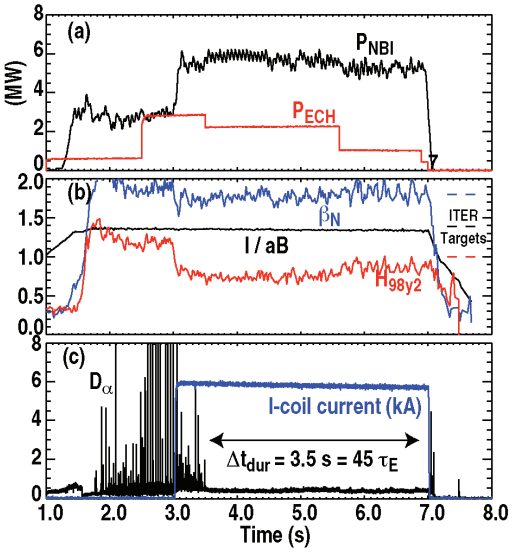

Fig. 1. Demonstration of n=3 RMP ELM Suppression at ITER baseline parameters: (a) Neutral beam and ECH power, (b) I/aB, β_N, H_{98y2}, (c) I-coil current and divertor D_α. ITER targets are shown as dashed lines in (b).

Separate DIII-D experiments have demonstrated the ability of using n=2 RMPs to achieve ELM suppression at low $\nu^*_{e\,ped}$ [4]. In these experiments, the applied toroidal phase between the upper and lower I-coils $\Delta\phi_{ul}$ has a dramatic impact on ELM mitigation/suppression. Sustained ELM suppression was achieved with $\Delta\phi_{ul}$=0° (equivalent to even parity in the n=3 case) and $\Delta\phi_{ul}$=-30° at fixed q_{95}=3.75. Periods of suppression have also been observed for $\Delta\phi_{ul}$ = +15° during discharges employing a ramp of the plasma current to vary q_{95}. In constrast, with $\Delta\phi_{ul}$ = -60°, only ELM mitigation (significantly smaller ELMs but not suppression) was found, while with $\Delta\phi_{ul}$ = +75°, there was no impact on the ELM activity. Analysis indicates that the $\Delta\phi_{ul}$ dependence is more consistent with ideal MHD response than the vacuum response.

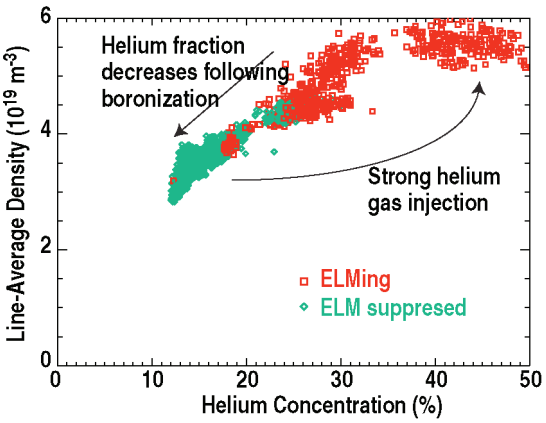

Fig. 2. Correlation of plasma density, helium concentration, and ELM suppression for a series of discharges following boronization. Multiple time slices per discharge are included.

3. Plasma Response to RMPs

The physics of the tokamak plasma response to applied 3D fields is complex, especially in the edge region where large variations in the plasma resistivity and rotation occur over small spatial scales. For regions in which the resistivity is high or the rotation low, the applied magnetic field "penetrates" the plasma column, with the resulting field being the simple addition of the 3D applied field and the 2D equilibrium field. Theory indicates that the motion of the electron fluid across the field lines at the

resonant surfaces determines the level of field "penetration" [5]. This velocity can be written as $\omega_{\perp e}=\omega_E+\omega_{*e}$, where $\omega_E=E_r/RB$ is $E\times B$ frequency, $\omega_{*e}=p'_e/enRB$ is the electron diamagnetic drift frequency (the prime denotes the radial derivative). Here, $E_r=V_{\theta Z}B_\phi-V_{\phi Z}B_\phi-V_{*i}B_T$ is the radial electric field that can be inferred from measurements of impurity fluid poloidal $V_{\theta Z}$ and toroidal velocities $V_{\phi Z}$ and ion diagmetic drift $V_{*i}=p'_Z/Z_ienB$. As the resistivity decreases and electron fluid velocity increases, shielding currents can form on rational surfaces (i.e., those where the safety factor $q=m/n$) as a result of high conductivity on these surfaces and the modulation of the local field in the plasma frame resulting from the plasma rotating past the fixed applied field. Ideal MHD theory predicts that such shielding currents completely screen the applied fields at the rational surface, leading to no resonant radial perturbations on that surface. It should be noted however that the presence of these shielding currents lead to increased non-resonant fields near this surface which can themselves have an effect on plasma transport. In regions where the resistivity is high and the electron fluid velocity low, resistive MHD codes predict "penetration" of the applied fields to the rational surfaces, leading to formation of magnetic islands. Additional complexities are introduced by finite β effects that lead to coupling of the applied field to the most unstable plasma modes (typically edge kink), potentially leading to amplification of these modes.

Evidence exists from recent DIII-D experiments that all of these effects are important in the overall plasma response with vacuum effects dominating in the scrape-off layer (SOL), ideal MHD response dominating in the high gradient region, and 2-fluid, resistive effects playing a key role near the top of the pedestal. The experiments to be described here were universally performed in the ITER-design shape cross section, scaled down by a factor of 3.7, referred to as the ITER Similar Shape (ISS) utilizing strong divertor exhaust to approach ITER-like pedestal collisionalities ($\nu^*_{e\_ped}<0.1$). These experiments have taken advantage of DIII-D's edge diagnostic suite and capability to vary the RMP spectrum (n=3 from one or two internal rows of coils, n=2) as well as toroidal phase variations of n=3 and n=2 RMPs to increase the toroidal coverage possible with fixed-location diagnostics.

Even as the simplest of descriptions of the tokamak plasma response to 3D fields, the vacuum model is predicted to be quite complex. Small non-axisymmetric perturbations lead to the splitting of the magnetic separatrix forming so-called homoclinic tangles near the separatrix [6]. In the divertor region, these tangles take the form of plasma lobes that create complex, yet predictable changes to the separatrix topology. The exact structure of these lobes is dependent on the magnetic geometry and the relative pitch of the equilibrium field lines and that of the applied 3D fields. Previous measurements of heat and particle flux patterns in the divertor of DIII-D have shown splitting of the strike-point on DIII-D [7,8], providing indirect evidence of the existence of these lobe structures. More recent DIII-D measurements utilizing tangential imaging of extreme ultra-violet (EUV) and soft x-ray (SXR) emission in the divertor region provide even more convincing evidence of the lobe structures near the X-point [Fig. 3(a–c) [9]. The images in Fig. 3 were constructed by taking the difference between two images obtained in otherwise identical plasma conditions with the n=3 RMP phase shifted toroidally by 60°, providing the maximum contrast in the toroidal direction. Lobes of emission are clearly observed. Interestingly, the spacing of the lobes on the high field side compress vertically as q_{95} is decreased while the lobes on the low field side do not change appreciably. These observations are qualitatively consistent with "forward" modeling that uses the TRIP3D-MAFOT [10] field-line tracing code and the diagnostic geometry to derive a synthetic diagnostic image [shown in Fig. 3(d–f)], assuming constant emission along a field-line. Additional evidence of the existence of these lobes is the observation of large decreases in

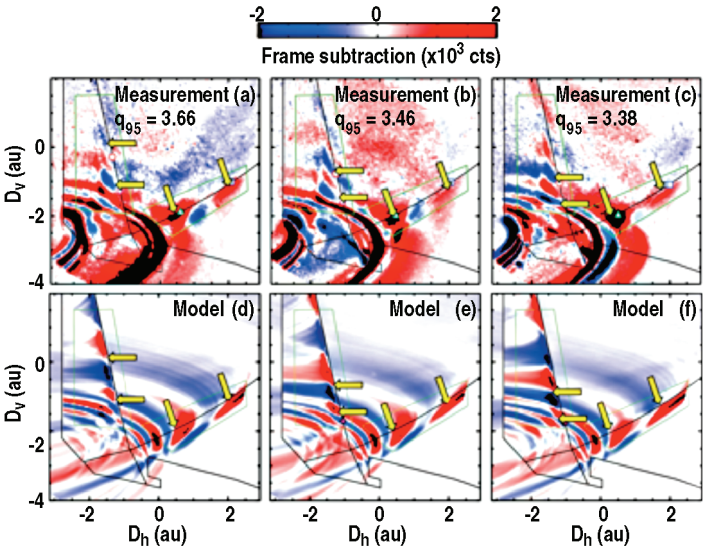

Fig. 3. (a,b,c) Measured and (d,e,f) modeled 2D images of the difference between soft X-ray emission taken with the n=3 RMP phase shifted toroidally by 60 degrees as a function of q_{95}. The locations of specific lobes are denoted by the yellow arrrows.

the floating potential measured by divertor Langmuir probes when these lobes intersect the location of a probe. The measured voltages (~100 eV) are consistent with the presence of hot electrons that may travel along open field lines from the near edge and pedestal region to the divertor target [11].

While the vacuum model predicts substantial changes to the X-point and divertor regions, only small changes are predicted near the midplane on the low-field side for both n=2 and n=3 RMP applied fields. For example, TRIP3D-MAFOT predicts that the toroidal variation of the locations of the stable and unstable manifolds (the homoclinic tangles associated with the separatrix) only vary by ~1 cm torodially for both n=2 and n=3 RMPs. Because of diagnostic limitations due to toroidally fixed measurement locations, comparisons to these predictions require varying the toroidal phase of n=2 and n=3 RMPs during otherwise similar conditions. Note that because the I-coil set in DIII-D consists of 6 toroidal segments, only two phases of an n=3 RMP can be applied (shifted by 60° relative to each other) while the n=2 RMP can be continuously rotated toroidally, albeit with some changes occurring in the n=2 RMP spectrum.

Utilizing such toroidal phase shifts/rotations, the displacement of the outer edge region can be inferred from several different measurements at various toroidal angles [neutral beam-induced beam emission spectroscopy (BES) measured by a tangential camera (145°), reflectometer density profile (255°), and charge exchange recombination (CER) C VI emission (325°) all at the outboard midplane]. An example of the data obtained from these diagnostics as the n=2 is rotated toroidally at 5 Hz is shown in Fig. 4. In this case, the radial displacement inferred from each of these measurements is ~2.5 cm. The three data sets taken together reveal the toroidal structure of the perturbation. The beam emission spectroscopy (BES) and CER measurements show nearly the same time response, as is expected since these measurements are separated by 180°. The reflectometer data confirms the n=2 structure with it occurring at ~65% of the n=2 cycle, consistent with its toroidal displacement (110°/180°) from the BES/CER measurements. The magnitude of the response as the n=2 RMP is rotated is significantly larger than that predicted by TRIP3D-MAFOT [12]. Similar measurements taken with n=3 RMP toroidal phase shifts of 60° show much smaller edge displacments (<1 cm). The apparent strong dependence on the toroidal mode number of the applied RMP suggests that the ideal MHD response may be playing a significant role in the observed n=2 displacements. This is consistent with the expectation that the magnitude of the ideal response scales inversely with toroidal mode number.

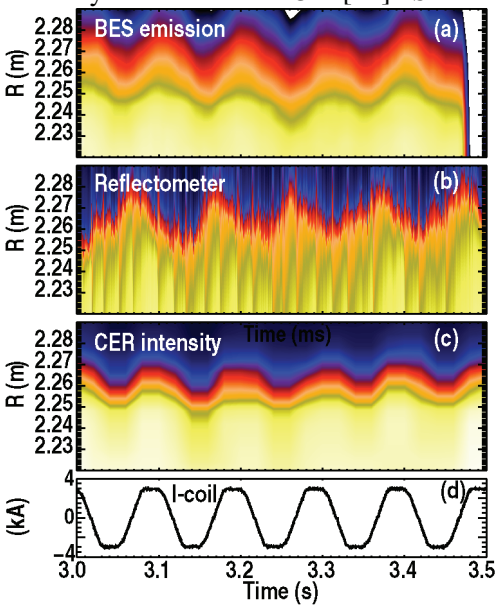

Fig. 4. Temporal evolution of (a) BES emission; (b) reflectometer density; and (c) CER intensity profiles as (d) an n=2 RMP is rotated toroidally at 5 Hz.

The above discussion has focused on the generic plasma response when edge-resonant RMPs are applied. Previous results from DIII-D have shown a strong sensitivity to q_{95} with ELM suppression *typically* observed for 3.4 <q_{95}<3.55. Vacuum modeling suggests that this q_{95} range is near the value in which vacuum island overlap occurs in the edge region (at typical RMP perturbation levels). However, modeling suggests a much broader maximum in the island overlap criterion with q_{95}. Although the RMPs do affect a density response over a very broad range in q_{95}, the narrow region of ELM suppression suggests that there is more physics at play than the vacuum interaction.

Detailed profile analysis of data taken during fine-scale q_{95} scans around the *typical* q_{95} window for ELM suppression (3.4<q_{95}<3.55) indicate that while the edge n_e response is comparable for all q_{95} values, the edge T_e response is quite dependent on q_{95}. Figure 5 shows the RMP-induced change in the pedestal n_e and T_e and the n_e, T_e, p_e widths during the RMP phase. The data here is a time average (over 600 ms during stationary conditions) of the inferred pedestal parameters using TANHFIT analysis of Thomson scattering data. The largest response to the applied RMP is that of pedestal n_e (~40% in this case) with the width of the density pedestal nearly unchanged as q_{95} is varied. While the pedestal T_e response is significantly smaller than the n_e response, a clear q_{95} dependence is evident during the RMP with a much larger T_e response observed as q_{95} decreases. Interestingly, within the data resolution available, the pedestal T_e width reaches a minimum within the q_{95} ELM suppression window. More data is required at low q_{95} to confirm this. These

changes lead to pedestal widths in the q_{95} ELM suppression window that EPED1 [13] pedestal modeling predicts should be peeling-ballooning stable.

It is also important to note that long-wavelength ($k_\perp \rho_i < 1$) turbulence responds very rapidly as the n=3 RMP is applied [13]. Shown in Fig. 6 is the frequency resolved time history of n_e fluctuations as measured by BES near the top of the pedestal. Quite evident from this figure is the increase in density fluctuations below ~100 kHz as the RMP is applied and the marked difference in the magnitude of the fluctuations during the RMP ELM suppressed phase relative to the phase between ELMs prior to RMP turn-on. Experiments using rapid amplitude modulations in the applied n=3 RMP have shown that the n_e fluctuations increase prior to changes in the background density measured at the same location. This suggests that the RMP has a direct effect on edge plasma turbulence, most likely through rapid changes in the magnetic topology in this region. These changes in fluctuation amplitude are localized near the pedestal top ($0.88<\rho<0.92$) while in the pedestal itself ($\rho \sim 0.98$), fluctuations are not strongly affected. Fluctuation amplitudes change occur over a wide range in q_{95}, similar to the density response decribed earlier, suggesting a link between RMP-induced turbulence and the ubiquitous density decrease observed with RMPs.

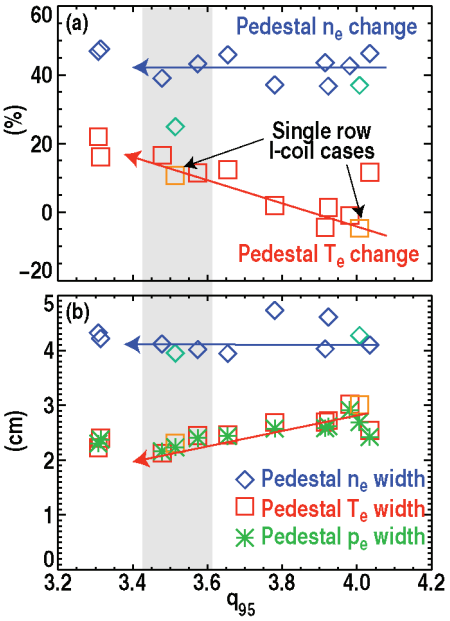

Fig. 5. Variation of (a) percentage decrease in pedestal n_e and T_e due to n=3 RMP and (b) resulting n_e, T_e, and p_e pedestal widths as q_{95} is varied. Shading shows the observed ELM suppression.

Utilization of the 60° toroidal phase shifts of the applied n=3 RMP described earlier reveal that the response of the electron temperature to the perturbation is complex. Figure 7 shows the variation of the edge temperature profile as q_{95} is scanned over the range $3.8 < q_{95} < 3.2$. Most evident in Fig. 7 is the coherent response of the T_e near the Thomson location of Z_{TS}=72 cm. Based on EFIT reconstructions of the equilibrium, this location is very close to the plasma separatrix. The coherent nature of the oscillations in this region is suggestive of a kink-like helical deformation of the plasma flux surfaces by the RMP. The magnitude of this response is observed to decrease as q_{95} decreases, becoming quite small for q_{95}<3.4. Similar oscillations and variations are observed on the density profile measured by Thomson scattering and a range of other diagnostics. A second striking (and perhaps more important) feature evident in Fig. 7 is the 90° phase difference in the response for Z_{TS}<70 cm to the response for Z_{TS}>71 cm between 3.0 and 4.2 s. This time range corresponds to a q_{95} range of 3.55→3.3, the typical range over which ELM suppression is observed. The flattening and steepening of the profile as the n=3 phase is changed is similar to that which would be expected if an island was centered near Z_{TS}=70 cm. Toroidally displaced measurements such as those in Fig. 4 confirm the n=3 variation at the very edge. However, this data is insufficient to discriminate between island-driven transport and a response governed by a kink-like displacement at the very edge accompanied by a global change of transport inside the pedestal region. This is discussed in detail in the following section.

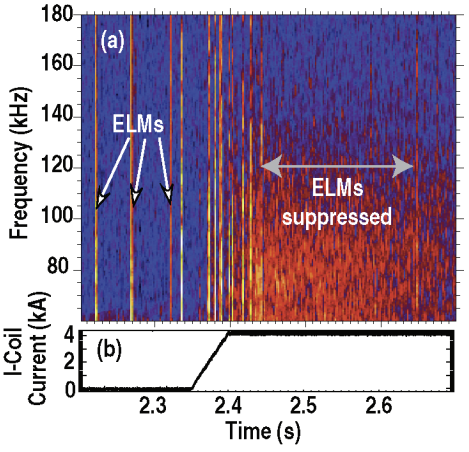

Fig. 6. Spectrogram of the BES-measured density fluctuations near the pedestal top as an n=3 RMP is applied.

4. Emerging Model for ELM Suppression and Supporting Data

There are several key observations from DIII-D experiments (e.g., large temperature gradient in edge region, small q_{95} window, dependence on β) that suggest a more extensive theoretical model is needed beyond the vacuum model to describe the experimental results. A key aspect of any theory that describes RMP ELM suppression is its consistency with existing theoretical descriptions of edge

transport and stability *without* RMPs present. The most advanced and benchmarked of these descriptions is the EPED model [14] that describes the pedestal evolution as simultaneously transport-constrained by kinetic-ballooning modes (KBMs) and stability-constrained by moderate *n* peeling-ballooning modes. A key feature of this model is the gradual expansion of the pedestal until a peeling-ballooning mode is encountered. A recent theory put forth by Snyder et al. [13] postulates that RMP-induced island formation near the top of the pedestal region could inhibit growth of the pedestal width, arresting the pedestal evolution at a stable operating point below the peeling-ballooning stability limit.

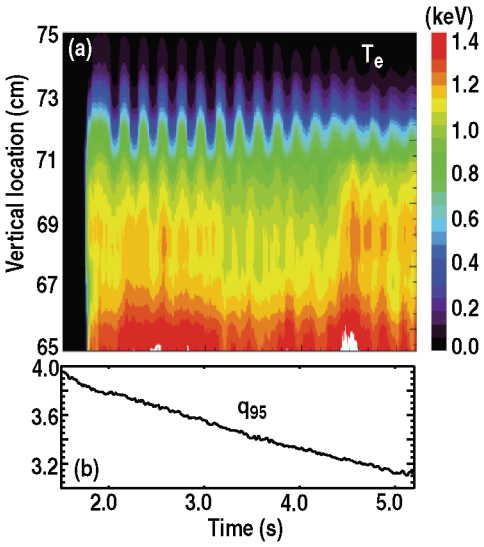

Fig. 7. Temporal evolution of the T_e profile measured by Thomson scattering during a q_{95} ramp as the n=3 RMP phase is varied by 60°.

A key component of this model is the realized resonant magnetic perturbations in the edge region. Profiles of resistivity and electron fluid velocity of a typical RMP ELM suppressed discharge in DIII-D are shown in Fig. 8(a). Based on the description in Sec. 1, one would anticipate that the SOL and far edge region (ψ_N>0.99) will be dominated by vacuum field effects due to the high resistivity and low rotation of the plasma. In the near edge region (0.95<ψ_N< 0.99), the high electron fluid velocity (resulting from diamagnetic effects associated with the large pressure gradient in this region) and moderate resistivity should result in shielding of the applied fields and small or non-existent magnetic islands. In the pedestal region (ψ_N<0.9), the competition between the ion toroidal rotation and the electron diamagnetic drift leads to a zero-crossing of the electron fluid velocity in this region, potentially opening up the possibility of penetration of the applied field and magnetic island formation. In the latter two regions, the overall response may be strongly affected by coupling of the applied perturbations with stable, ideal MHD eigenmodes of the plasma. The strength of this response is dependent on the stability index of the most unstable modes and is therefore strongly enhanced as the pressure gradient or equivalently β is increased. Figure 8(b,c) provides an example of the predicted impact of these various effects on the effective magnetic perturbation (and island size), in this case computed by the M3D-C1 resistive MHD code [5]. In the vacuum case, the effective resonant field falls from the plasma edge, reflecting the approximate $(R_{coil}\text{-}R)^{-m}$ expectation of the falloff of this field. As two-fluid and resistive effects are added to the model, the resonant field is comparable (actually larger in this case due to some amplification of the field) to the vacuum applied field but falls off strongly on either side of the $\omega_{\perp e}$=0 crossing. This has the net effect of producing large islands near the top of the pedestal with very small islands in the high gradient edge region and in the core region.

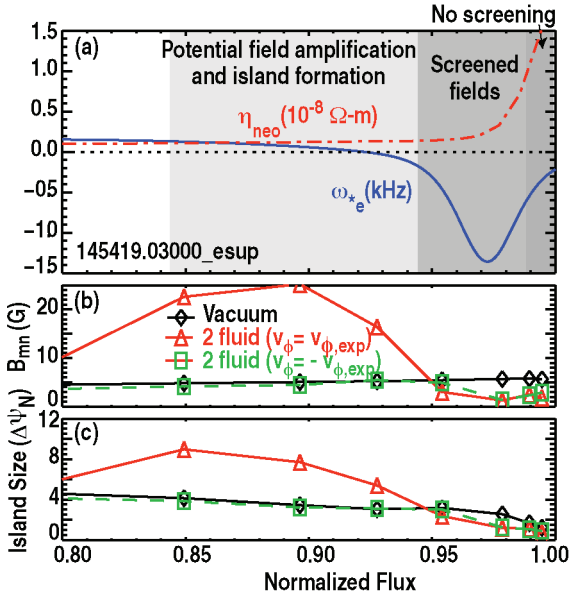

Fig. 8. Profiles of (a) resistivity and $\omega_{\perp e}$; M3D-C1/SURFMN computed (b) field perturbation and (c) island size for typical RMP ELM suppressed case (q_{95} = 3.45).

Survey data from a series of DIII-D discharges with *n*=3 RMP applied are supportive of this premise. Shown in Fig. 9 is the observed ELM frequency in a series of discharges in which q_{95} was varied systematically to vary the expected location of the vacuum islands in the pedestal region. The ordinate in this figure is the radial distance (measured in normalized flux) between the top of the pedestal (inferred from TANHFIT analysis) and the SURFMN outer edge of the *m*=10/*n*=3 island. Positive values of this parameter indicates that the pedestal top is farther out than the outer edge of the *m*=10/*n*=3 island. A clear correlation is observed between the pedestal-island gap and the ELM frequency with ELM

suppression occurring only in cases where this gap approaches zero. This suggests the possibility that island formation is in fact limiting further expansion of the pedestal, leading to ELM suppression.

Further evidence of island-like transport effects was shown above in Fig. 7. Under the assumption that the observed changes in the profile are due entirely to an n=3 displacement of the plasma column, one can infer the displacement as the radial distance between the nearest locations of the same temperature on each profile (as in Fig. 10 inset). Such analysis is shown in Fig. 10. The displacement (expressed in terms of normalized flux) in this case is inferred from detailed profile analysis of the Thomson scattering T_e measurements of the pedestal region in discharges with fixed q_{95} and a 10 Hz modulation of the toroidal phase of the n=3 RMP by 60°. To improve statistics, profiles for the two phases of the RMP are constructed by taking a time-average of all the data taken during a particular toroidal RMP phase. Data near the time of observed ELMs are excluded from this average. Figure 10 reveals several interesting features. First, there is a universal displacement at the edge that decreases as q_{95} increases (consistent with the observations in Fig. 7). Secondly, a clear displacement inversion layer is observed near the region $0.9<\psi_N<0.95$ in all cases with a clear correlation between the location of this inversion layer and the expected location of the m=10, n=3 island computed by SURFMN. Finally, the magnitude of the observed inward displacement is quantitatively consistent with the computed size of the m=10, n=3 island (~2% of the normalized poloidal flux).

While the observations are consistent with expectations if an island is present, there are other possibilities for the observed profile effects. The primary alternate explanation is that the effects are caused by a kink-like displacement at the very edge accompanied by a global change of transport inside the pedestal region. There is clear evidence from these discharges of a global change in β_N and density as the toroidal phase of the n=3 RMP is changed (Fig. 11). In addition, rotation measurements at the same radial location at the top of the pedestal but toroidally displaced by 60° exhibit concurrent modulations with the changes in the RMP phase, suggesting a toroidally symmetric response. Subsequent analysis and experiments on DIII-D suggests that this effect may be due to intrinsic n=3 error fields that interact with the applied RMP field to produce a modulation in the transport. In fact, Fig. 11 shows that by applying an approximate 1.0 kA offset on one phase of the n=3 RMP, the modulation in β_N and toroidal rotation can be reduced significantly. Analysis of the few discharges that have been produced with the 1.0 kA offset show significantly reduced levels of the apparent displacement in the core region, suggesting that this effect is a large source of the observed displacement inside ψ_N=0.9. However, within the uncertainties, an inversion layer is still observed (case with dotted line in Fig. 10), again indicating that the magnetic topology is leading to island-like transport effects at the top of the pedestal.

The most straightforward test of the importance of the $\omega_{\perp e}$=0 crossing in obtaining ELM suppression is to utilize counter-NBI

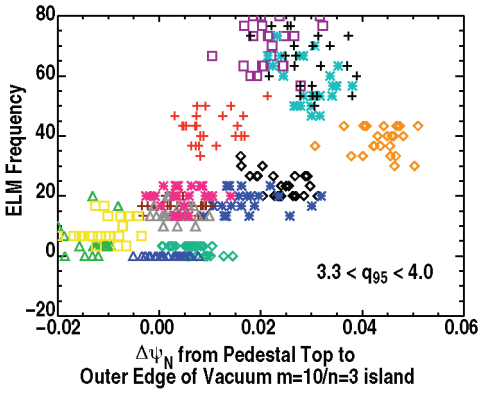

Fig. 9. ELM frequency vs the gap between the pedestal top and the computed outer edge of the m=10/n=3 island. Colors indicate different shots during a q_{95} scan.

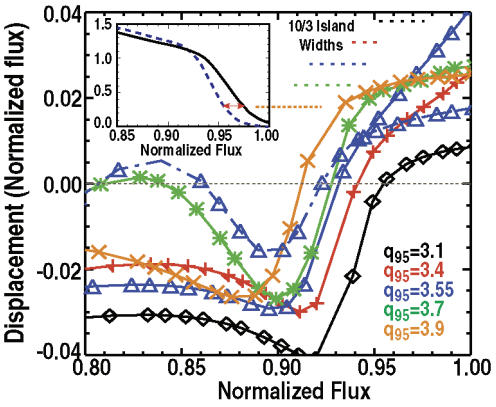

Fig. 10. Radial profiles of T_e (inset) and inferred displacement in the edge region due to 60° toroidal phase shift in the n=3 RMP field for various q_{95} levels. Solid lines are with no n=3 offset applied to RMP. Dashed line is q_{95}=3.5 case with 1 kA offset applied. Dotted lines represent the island location and width calculated by SURFMN.

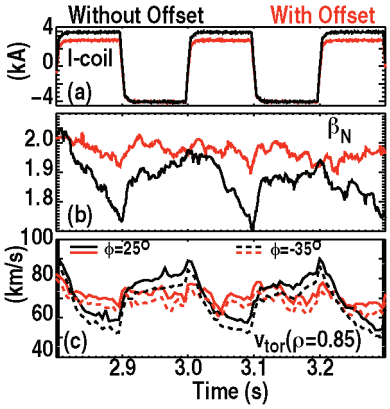

Fig. 11. Temporal variation of (a) I-coil current; (b) β_N; and (c) toroidal rotation at ρ=0.85 for two toroidal locations with and without a 1 kA offset applied to the applied RMP.

such that the V_{ExB} and diamagnetic drifts are in the same direction, thereby eliminating the possibility of a $\omega_{\perp e}=0$ crossing. This is illustrated in Fig. 8 above in which the toroidal rotation simply reversed (green) shows substantial screening in the edge region and much lower amplifcation in the pedestal region. The experimental test of this prediction was carried out utilizing a standard discharge that routinely provides RMP ELM suppression with co-NBI operation. As in the co-NBI case, strong divertor exhaust is utilized in the counter-NBI case to access pedestal n_e and levels in which ELM suppression is generally observed with co-NBI. For the two time slices compared in Fig. 12, there are very modest changes in $|I_p|$ and B_T (<3%), but both cases have the same q_{95}=3.4. In addition, n_e and β_N are nearly identical. As expected with counter-NBI, the toroidal rotation leads to $\omega_{\perp e}<0$ everywhere as shown in Fig. 12(b). While some ELM mitigation occurs with counter-NBI near the co-NBI q_{95} window for ELM suppression, ELMs are still present, suggesting the importance of the $\omega_{\perp e}=0$ crossing in ELM suppression.

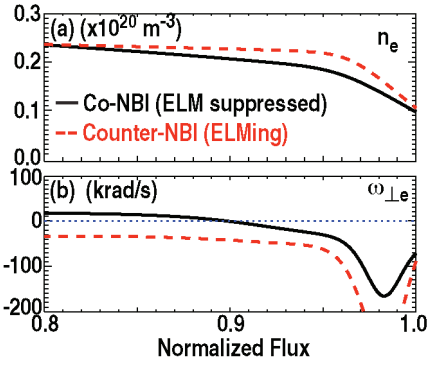

Fig. 12. Radial profiles of (a) density and (b) $\omega_{\perp e}$ in comparable discharges with co- (black) and counter- (red) NBI.

Finally, evidence of helical structures inside the plasma edge has been observed via tangential imaging of SXR emission using the same technique described in Sec. 2 but with a higher energy filter (~600 eV) installed to accentuate sensitivity to emission from the confined plasma. Figure 13 shows a tomographic inversion of the difference in measured emission with the n=3 RMP phase shifted toroidally by 60° along with the M3D-C[1] prediction of the soft x-ray emission. Clear evidence exists for the presence of helical structures. While the radial location of these structures is consistent with the ψ_N=0.98 surface [Fig. 13(a)], the curvature traced out by these structures poloidally is more consistent with a flux surface further in (e.g., ψ_N=0.95). More comparisons between theory and measurements are required to resolve this issue.

To conclude, extensive studies on DIII-D have identified many elements of an emerging model to explain RMP ELM suppression and extend its operational range, providing increased confidence in its applicability in ITER.

This work was supported by the US DOE under DE-FC02-04ER54698, DE-AC02-09CH11466, DE-FG02-89ER53296, DE-FG02-08ER54999, DE-FG02-07ER54917, DE-FG02-08ER54984, DE-AC52-07NA27344, DE-AC05-00OR22725, and DE-AC04-94AL85000.

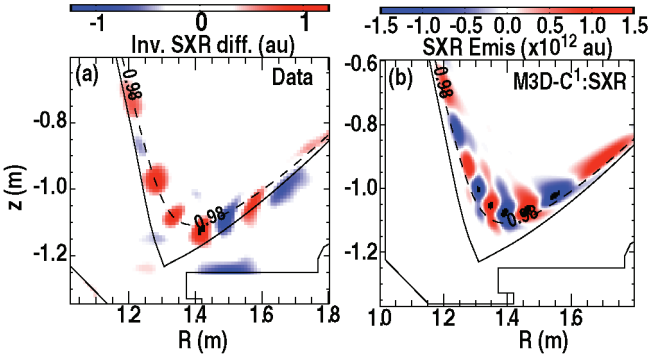

Fig. 13. Difference of SXR emission as n=3 RMP toroidal phase is varied by 60° and (b) tomographic inversion assuming constant emission along a field line.

References

[1] LOARTE, A., et al. "ITER ELM control requirements, ELM control schemes & required R&D," Proceedings of the 2010 IAEA Fusion Energy Conference, Daejeon, Republic of Korea, paper ITR/1-4.
[2] EVANS, T.E., et al., Nature Physics **2** (2006) 419
[3] FENSTEREMACHER, M.E., et al., Phys. Plasmas **15** (2008) 056122
[4] LANCTOT, M.J., et al., "Sustained Suppression of Type-I Edge Localized Modes with Dominantly n=2 Magnetic Fields in DIII-D," to be submitted to Nucl. Fusion (2012)
[5] FERRARO, N.M., Phys. Plasmas **19** (2012) 056105
[6] EVANS, T.E., et al., Contrib. Plasma Phys. **44** (2004) 235
[7] JAKUBOWSKI, M.W., et al., Nucl. Fusion **49** (2009) 095013
[8] SCHMITZ, O., Plasma Phys. Control. Fusion **50** (2008) 124029
[9] SHAFER, M.W., et al., "Experimental Imaging of Separatrix Splitting on DIII-D," submitted to Nucl. Fusion (2012).
[10] WINGEN, A., et al., Phys. Plasmas **16** (2009) 042504
[11] WATKINS, J.G., et al., J. Nucl. Mater. **363-365** (2007) 708
[12] MOYER, R.A., et al., "Measurement of Plasma Boundary Displacement by n=2 Magnetic Perturbations Using Imaging Beam Emission Spectroscopy," submitted to Nucl. Fusion (2012)
[13] McKEE, G.R., et al., this conference.
[14] SNYDER, P.B., et al. Phys. Plasmas **19** (2012) 056115